ACS Energy LETTERS

http://pubs.acs.org/journal/aelccp

Operando Label-Free Optical Imaging of Solution-Phase Ion Transport and Electrochemistry

James K. Utterback,* Alex J. King, Livia Belman-Wells, David M. Larson, Leo M. Hamerlynck, Adam Z. Weber, and Naomi S. Ginsberg*

Cite This: *ACS Energy Lett.* 2023, 8, 1785−1792

Read Online

ACCESS | Metrics & More | Article Recommendations | Supporting Information

ABSTRACT: **Ion transport is a fundamental process in many physical, chemical, and biological phenomena, and especially in electrochemical energy conversion and storage. Despite its immense importance, demonstrations of label-free, spatially and temporally resolved ion imaging in the solution phase under *operando* conditions are not widespread. Here we spatiotemporally map ion concentration gradient evolution in solution and yield ion transport parameters by refining interferometric reflection microscopy, obviating the need for absorptive or fluorescent labels. As an example, we use an electrochemical cell with planar electrodes to drive concentration gradients in a ferricyanide-based aqueous redox electrolyte, and we observe the lateral spatiotemporal evolution of ions via concentration-dependent changes to the refractive index. Analysis of an evolving spatiotemporal ion distribution directly yields the diffusivity of the redox-active species. The simplicity of this approach makes it amenable to probing local ion transport behavior in a wide range of electrochemical, bioelectronic, and electrophysiological systems.**

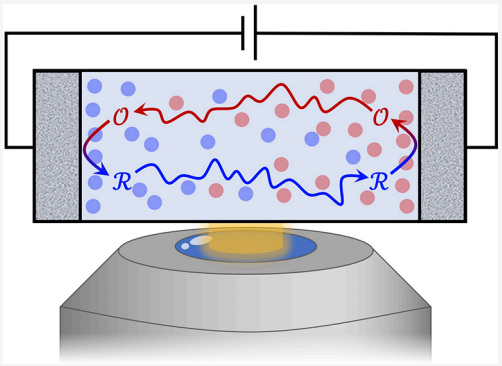

Achieving a detailed picture of ion transport in the solution phase under (electro)chemically active conditions remains a major challenge that limits advances in applications ranging from solar fuel conversion and bipolar membranes to the understanding of electrophysiology.[1−4] Ion transport is a multiscale problem of diffusion and electrostatics that is dictated by nanoscale solvent structuring, mesoscale impacts of local environmental structure, and microscale transport.[5,6] Typically, ion transport within electrochemical systems is probed indirectly with bulk measurements of voltage and current, leaving the species concentration profiles and transport properties to be inferred through modeling and simulations.[7−9] There exist powerful techniques for probing electrode and electrolyte structure or steady-state ion distributions,[10−20] and absorptive and fluorescent labels as well as Raman-active modes have been used to probe ion transport with high resolution in specific cases,[9,21−32] but there is an outstanding need for direct universal measurements of ion transport in native microenvironments with spatiotemporal resolution. Optical detection of electrochemical processes via voltage-induced refractive index changes at electrodes also has a long history[11−13,33−36] and has more recently been used for imaging electrochemical processes at electrode−electrolyte interfaces,[35−39] electric double layer dynamics,[40] and ion intercalation in battery electrodes.[41] Nevertheless, dynamic *operando* measurements of ion transport in solution that do not depend on optical resonances, Raman-active modes, or ion proximity to an electrode surface or plasmonic structures remain difficult. Although they generally lack readily accessible optical signatures, ionic species do in general perturb the refractive index of their environments. The primary challenge of this contrast mechanism is the fact that solution-phase ionic species typically introduce a relatively small perturbation to the solution's refractive index.[42,43] For example, steady-state electrochemically induced ion gradients have been detected long ago but required prolonged integration times.[11−13] Therefore, to observe and extract the *dynamics of ion transport* requires detecting the small changes to a solution's refractive index as a function of position with sufficient time resolution.

Received: January 17, 2023
Accepted: March 7, 2023
Published: March 16, 2023

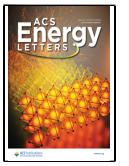

As a result, a universal *operando* approach for imaging ion dynamics in solution with sufficient spatiotemporal resolution has remained elusive.

Here we refine interference reflection microscopy[35,36,44,45] to spatiotemporally resolve electrochemically induced ion concentration gradient evolution in solution with sub-mM, sub-μm, and ms sensitivity without using additional labels or electrode enhancement effects. *Operando* experiments are achieved with an electrochemical cell compatible with optical microscopy such that the solution between parallel vertical electrodes can be observed under applied bias. Electrochemical reaction-induced concentration changes of an aqueous ferricyanide-based redox electrolyte cause measurable changes in the reflectance at the coverslip−solution interface down to $\sim 10^{-4}$ on a CMOS camera. Spatiotemporally resolving the evolution of the concentration gradients that develop between the electrodes via wide-field imaging directly yields the diffusivity of the redox-active ions in solution. Because measurements are made off-resonantly far from any optical absorption peaks, the observed signal is due to the real part of the refractive index, suggesting a universal method to spatiotemporally resolve the transport of ionic species. Multiphysics continuum simulations corroborate the experiments and analysis, showing consistency with the measured signal amplitude and spatiotemporal dynamics.

To spatiotemporally measure ion transport in solution, we use interference reflection microscopy, which can detect small changes in the refractive index that occur due to voltage-induced changes in ion concentration. Wide-field imaging is achieved using an LED light source, a high numerical aperture oil-immersion objective, and a CMOS camera (Figure 1, see Supporting Information (SI) for further details). The light intensity on the camera is proportional to the reflectance R from the quartz−solution interface as a function of position and time. Thus, a normalized change in intensity in response to a change in solvated ion concentration is equal to the normalized change in reflectance, $\Delta R/R = (R - R_0)/R_0$, where R_0 is the reflectance before a perturbation is applied (i.e., applied voltage or static concentration change). To establish the method, we chose to use the model redox-active system of aqueous ferricyanide/ferrocyanide ($[Fe(CN)_6]^{3-}/[Fe(CN)_6]^{4-}$) with a supporting electrolyte of K_2SO_4—a very thoroughly documented system with well-understood reaction and transport properties.[6,46] Importantly, the light source is not resonant with the absorption feature of any species in solution (Figure S1) to demonstrate the generality of the approach. To generate ion concentration gradients and probe them *in situ*, we designed an electrochemical cell that features a microfluidic channel that has parallel Pt electrode walls (Figure 1, S2). The vertical electrodes extend 3 μm above the quartz−solution interface to the PDMS roof of the 2 mm-long channel; this geometry is designed to eliminate axial concentration gradients and render the mass transfer dynamics one-dimensional. Applying a voltage across the cell drives the reaction $[Fe(CN)_6]^{3-} + e^- \rightleftharpoons [Fe(CN)_6]^{4-}$ in the oxidative (reductive) direction at the anode (cathode) without changing the average concentrations throughout the system.

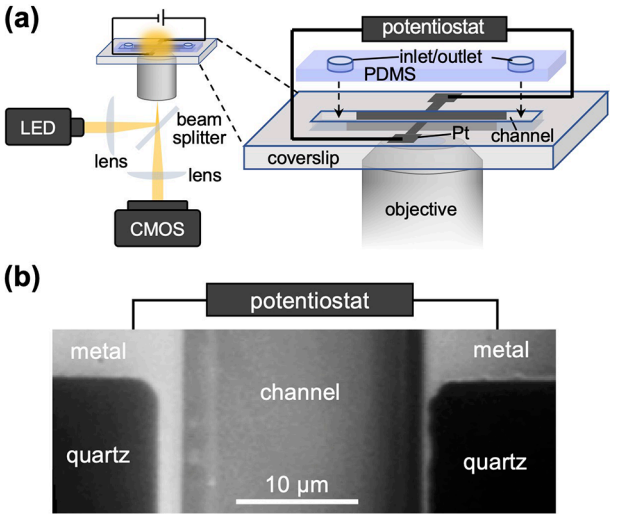

Figure 1. *Operando* interferometric reflection microscopy. (a) Measurement schematic and custom electrochemical cell. (b) Optical reflectance image of empty microfluidic electrochemical cell.

To calibrate the concentration-induced changes in reflectance, we measure $\Delta R/R$ of 595 nm light for static solutions on a coverslip as a function of ion concentration relative to R_0 for pure water. Droplets of solution containing a series of concentrations of dissolved salts are placed on a coverslip in air and we immediately measure the intensity on the camera while focusing on the coverslip−solution interface. $\Delta R/R$ decreases linearly with increasing concentration of K_2SO_4, $K_3[Fe(CN)_6]$, and $K_4[Fe(CN)_6]$—as well as when combined in equal parts—over the range measured (Figure 2a). This trend originates from the change in refractive index with solute concentration. At a wavelength of 595 nm, the absorbance of each species in solution is negligible (Figure S1); thus, the reflectance is dominated by the real part of the refractive index:

$$R \approx (n_{sub} - n_{soln})^2/(n_{sub} + n_{soln})^2 \quad (1)$$

where n_{sub} and n_{soln} are the real parts of the refractive index of the substrate (coverslip) and the solution, respectively. For relevant salt concentrations such as those used here,[5,6] the mole fractions are sufficiently small that the solution refractive index is well-known to change linearly with the solute concentration:[42,43]

$$n_{soln} = n_{water} + \sum_i K_i x_i \quad (2)$$

where n_{water} is the refractive index of the neat solvent, $x_i = [\text{solute } i]/([\text{solvent}] + \sum_i[\text{solute } i])$ is solute i's mole fraction, and K_i is a coefficient that is known to depend on the polarizabilities of the solvated species and the volume displacement they induce on the solvent.[42,43] By assuming (i) that each solute approximately contributes independently,[43] (ii) that $\sum_i K_i x_i \ll n_{sub}, n_{water}, |n_{sub}^2 - n_{water}^2|$, and (iii) that $[\text{solute } i] \ll [\text{solvent}]$, eqs 1 and 2 reduce to first order in $\Delta[\text{solute } i]$ to an expression for the ion-induced imaging contrast

$$\frac{\Delta R}{R} \approx -\frac{4n_{sub}}{(n_{sub}^2 - n_{water}^2)[\text{solvent}]} \sum_i K_i \Delta[\text{solute } i] \quad (3)$$

where the sum is taken over all solute species in solution. This expression fits the measured data in Figure 2a with high fidelity (see Table S1 for fitted values of K_i). eq 3 indicates that the total contrast is determined by the weighted sum of the $\Delta[\text{solute } i]$ with weights K_i while the nature of the substrate and solvent act as a prefactor that determines the sign and

https://doi.org/10.1021/acsenergylett.3c00129
ACS Energy Lett. 2023, 8, 1785−1792

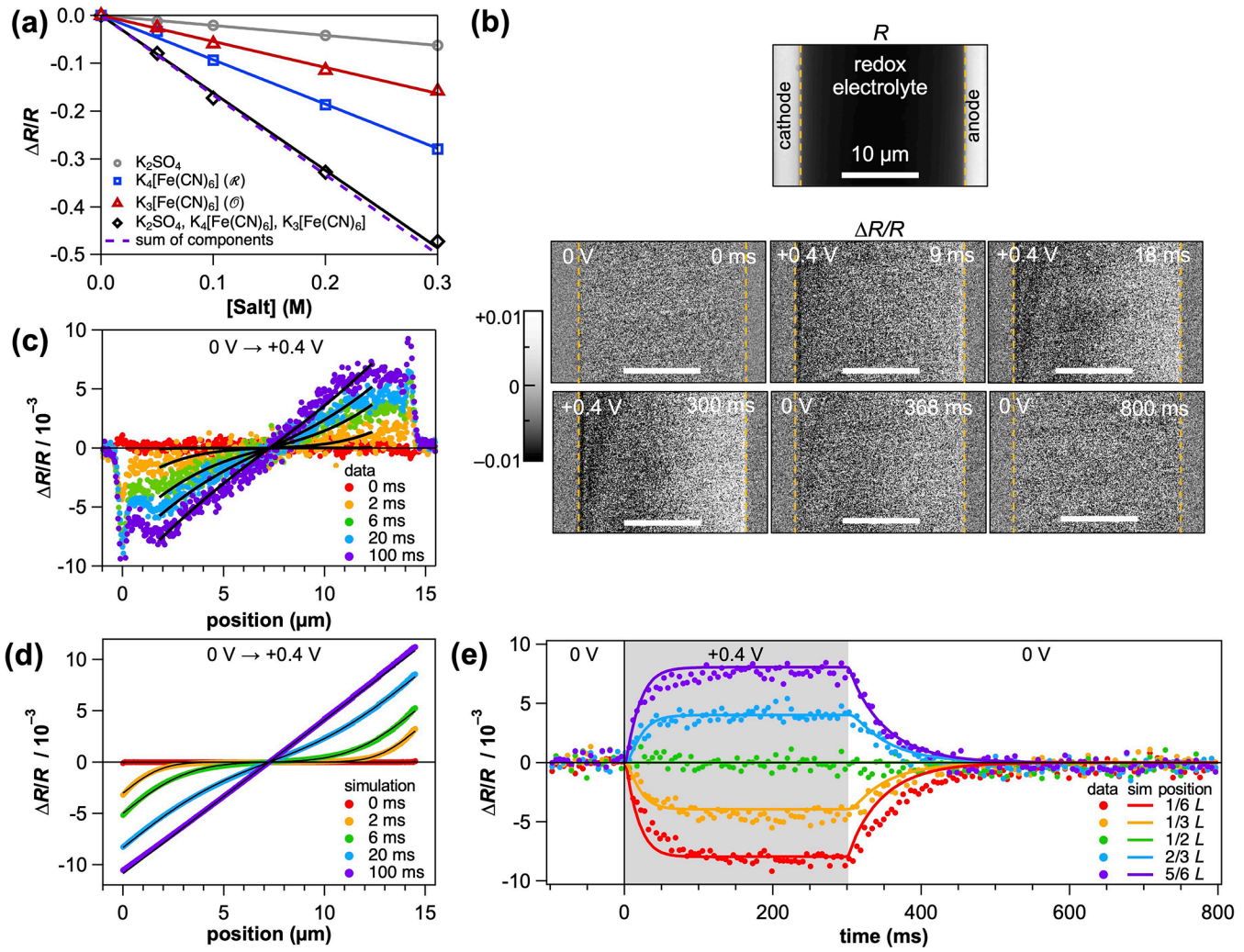

Figure 2. Optical detection of lateral ion transport. (a) Static measurement of change in reflectance with respect to solute concentration relative to neat water. (b) Raw reflectance image of microfluidic channel loaded with 100 mM $K_3[Fe(CN)_6]$, $K_4[Fe(CN)_6]$ and K_2SO_4, and $\Delta R/R$ time series before (top left), during (remaining top and bottom left frames) and after (bottom right) applying a voltage of +0.4 V across the cell. A voltage of +0.4 V was applied from t = 0 to 300 ms and was otherwise at ground. Right-hand electrode is the positive terminal (anode). Electrode edges are indicated with dashed yellow lines. (c) Profile of $\Delta R/R$ versus position as a function of time after applying +0.4 V at t = 0. Traces were averaged over 20 μm along the channel axis (vertical as pictured in (b)) and over 2 ms in time. Black curves show fits to eq 4. (d) Simulated $\Delta R/R$ profiles that parallel the experimental data in (c). Black curves show fits to eq 4. (e) Experimental (circles) and simulated (curves) time traces of $\Delta R/R$ at a series of 6 different positions between electrodes relative to the channel width L (horizontal as pictured in (b)). Experimental time traces were averaged 0.5 μm across the cell width and over 20 μm along channel axis.

modulates the magnitude of the contrast. For salts in solution, K_i is typically dominated by the anions because their polarizability is often larger than that of many cations.[13,43] Additionally, our simulations described below show that electrochemically induced Δ[solute i] is large for the redox-active species and relatively small for spectator ions under our experimental conditions (Figure S3). These two factors result in $\sum K_i \Delta$[solute i] being dominated by $[Fe(CN)_6]^{3-}$ and $[Fe(CN)_6]^{4-}$ in our measurements. Under these approximations, we use the data in Figure 2a and room temperature values of n_{sub}, n_{water} and [water] to estimate that $K_{K_4[Fe(CN)_6]} - K_{K_3[Fe(CN)_6]} \approx 1.8$ and find that, for equal and opposite changes in the concentrations of $[Fe(CN)_6]^{3-}$ and $[Fe(CN)_6]^{4-}$ in an electrochemical cell, eq 3 reduces to $\Delta R/R \approx -\alpha\Delta[[Fe(CN)_6]^{4-}] = +\alpha\Delta[[Fe(CN)_6]^{3-}]$, with $\alpha = \frac{4n_{sub}}{(n_{sub}^2 - n_{water}^2)[water]}(K_{K_4[Fe(CN)_6]} - K_{K_3[Fe(CN)_6]}) \approx 0.3\ M^{-1}$. Assuming the illumination is sufficiently coherent, the 12-bit detector sensitivity limit yields $\Delta R/R \sim 10^{-4}$, which permits sub-mM sensitivity to concentration changes in the present case.

Interferometric reflection microscopy is sensitive to electrochemically induced changes in ion concentration changes well away from the electrodes. The electrochemical cell was loaded with 100 mM $K_3[Fe(CN)_6]$, $K_4[Fe(CN)_6]$, and K_2SO_4 (Figure 2b). Below, $[Fe(CN)_6]^{3-}$ and $[Fe(CN)_6]^{4-}$ are referred to as $\mathcal{O}$ and $\mathcal{R}$, respectively. Experiments begin by collecting images at uniform concentration at equilibrium with no applied voltage and at open circuit, and >100 frames are averaged to serve as R_0 to calculate $\Delta R/R$. Upon applying a voltage of +0.4 V across the electrodes, $\Delta R/R$ increases near the anode and decreases near the cathode (Figure 2b). This behavior is expected for our system given the fact that $K_{\mathcal{R}} > K_{\mathcal{O}}$ (see eq 3, Figure 2a, Figure S4); thus, $\Delta R/R$ decreases (increases) near

https://doi.org/10.1021/acsenergylett.3c00129
ACS Energy Lett. 2023, 8, 1785−1792

the cathode (anode) where $O(\mathcal{R})$ reacts to produce $\mathcal{R}(O)$. One-dimensional $\Delta R/R$ profiles at 5 different times following the application of the voltage (Figure 2c), obtained by averaging images along the channel axis, show clear symmetric behavior of the gradient that develops between the electrodes. As seen in time traces collected with 1.5 ms time resolution for selected positions between the electrodes (Figure 2e, circles), the system reaches steady state within ~100 ms of the voltage being applied and relaxes back to the equilibrium state when the voltage is released. The corresponding current transient appears in Figure S5. Applying an alternating square wave of ±0.4 V peak-to-peak across the electrodes further confirms the assignment of the voltage-induced signal to changes in $[O]$ and $[\mathcal{R}]$, as it demonstrates a reversible process as expected for the reaction $O + e^- \rightleftharpoons \mathcal{R}$ (Figure S6). Such voltage-induced changes in $\Delta R/R$ are not observed when the cell is loaded with pure water or the supporting electrolyte K_2SO_4 alone (Figure S6). The diffraction-limited behavior near the electrodes is suggestive of electric double-layer formation or electrochemically induced surface plasmon resonance changes, which have been thoroughly treated in previous reports.[34,36,37,40] Here we focus on contrast and transport in the mass transport boundary layer that in general lies between the electric double layer and bulk solution.

To validate the interpretation that $\Delta R/R$ directly reflects ion gradient evolution in solution, we performed finite element simulations of the electrochemistry and mass transport. The one-dimensional model consisted of two parallel facing Pt electrodes (14.5 μm gap) in a 100 mM $K_3[Fe(CN)_6]$, $K_4[Fe(CN)_6]$, and K_2SO_4 electrolyte solution (see SI for details). Mimicking the conditions of the experiments, all species in solution began at uniform concentration, then a voltage of +0.4 V was applied for a duration of 300 ms, at which point the voltage was switched to zero. The simulations yield the concentrations of all species as a function of time and position (Figure S3), from which the experimentally observed $\Delta R/R$ was calculated according to eq 3 (Figures 2d,e, Figure S4). We tuned the exchange current density as the only fit parameter to obtain agreement between the experimental and simulated amplitudes of $\Delta R/R$ at steady state (see SI for details). There may be minor inaccuracies in the optical parameters used in eq 3 or in the simulation parameters because the model neglects the oxidation of Fe(II) with O_2 and because it uses physical parameters, such as the exchange current density and diffusion coefficients, that are only known approximately. Importantly, plots of the calculated $\Delta R/R$ reproduce the essential behavior seen experimentally. $\Delta R/R$ increases near the positive electrode and decreases near the negative electrode (Figure 2d)—approximately reaching steady state around 100 ms—and the system relaxes back to equilibrium after the voltage is turned off (Figure 2e, curves). The small discrepancies in the time traces at different positions across the width of the cell (primarily in the time constants associated with the red and orange locations on the left side of the channel) may be due to asymmetries in the cell that are not accounted for in the model. Thus, the simulations support the attribution of the origin of the $\Delta R/R$ signal as concentration-induced changes in the refractive index.

Because the spatiotemporal data directly reflects ion concentration gradient evolution, it provides quantitative information about the underlying ion transport behavior without relying on models *a priori*. Specifically, we obtain good fits (black curves) of the profiles in Figure 2c,d as a function of position across the cell x and time t using the empirical function

$$\Delta R/R(x, t) = A(t)(\mathrm{erf}[x/w(t)] - \mathrm{erf}[(L - x)/w(t)]) \quad (4)$$

for fixed L. This ansatz reflects one-dimensional diffusion of electrochemical reaction products away from each of the electrodes and the phenomenology of the Cottrell equation (Figure 3a).[5,47] The fit range in the experimental data is smaller than in the simulation data in order to avoid electrode-imaging effects (Figure 2c,d). In analogy to empirically obtaining the charge and thermal carrier mean-squared expansion (MSE) in semiconducting or conducting solids by fitting spatiotemporal transient optical microscopy data to a

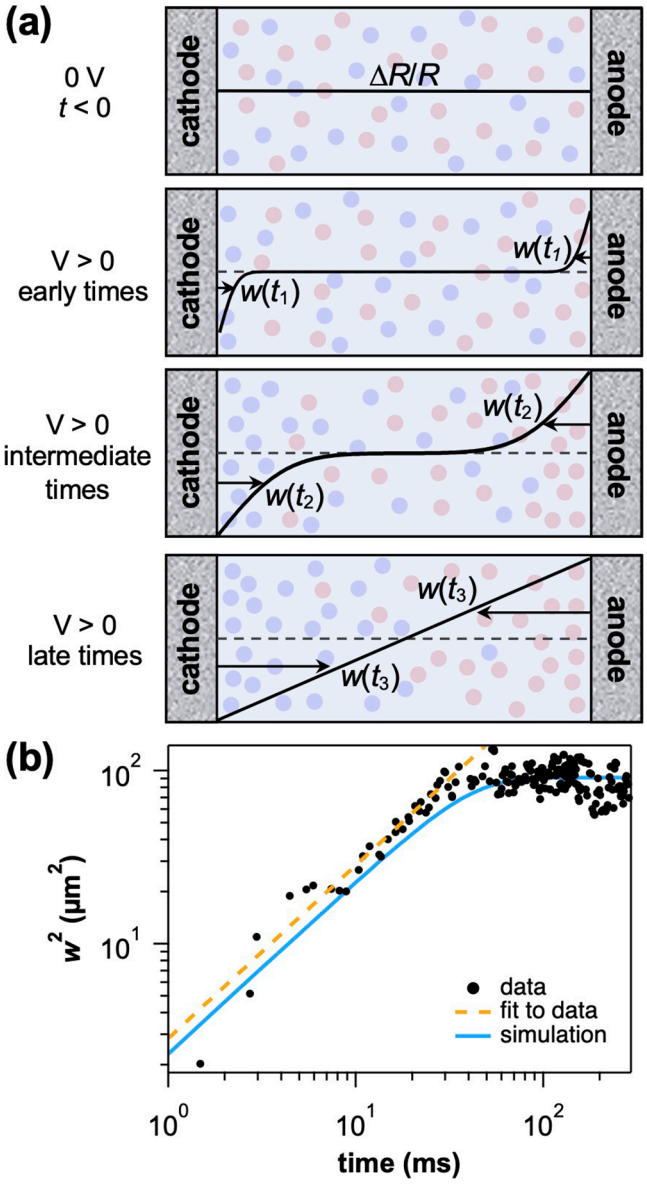

Figure 3. Model-free extraction of ion transport. (a) Schematic depiction of the mean-squared expansion of the ion concentration profile, characterized by the distribution's width w as it expands from each electrode. (b) Mean-squared expansion (MSE) of ions from the electrode surfaces calculated from data (black circles) and simulations (cyan curve). Data are fit to $w^2 = 4Dt$ (yellow dashed curve).

https://doi.org/10.1021/acsenergylett.3c00129
ACS Energy Lett. 2023, 8, 1785−1792

Gaussian of expanding width,[48−52] the fit parameter w in each error function here is a measure of the width of the ion profile being electrochemically generated and then expanding from the surface of each electrode (Figure 3a). We thus calculate the MSE as the temporal change in this width squared, $w^2(t)$, with $w^2(0) \simeq 0$ (Figure 3b, black circles). The experimentally obtained MSE appears linear over the first ∼35 ms, suggesting diffusive behavior, and then flattens out, as one would expect when approaching steady state for diffusion in a one-dimensional confined region, corresponding to the time scale on which the ionic species travel across the width of the channel. Indeed, eq 4 satisfies the diffusion equation in the case that $w^2(t) = 4Dt$, where the factor of 4 is expected for one-dimensional diffusion based on the error function definition. Fitting the MSE to this relationship (yellow curve) therefore gives $D = (7.2 \pm 0.3) \times 10^{-6}$ cm^2/s. Performing a similar analysis on the simulation data yields a very similar MSE (cyan curve). The small discrepancy between the experimental and simulated MSE curves could be due to slight mechanical drift in the microscope, the shot noise limit of the CMOS camera during *operando* measurement, assuming dilute solution theory and pure water transport in the simulation, or inaccuracies in the ion diffusivities from the literature used as parameters in the simulations. Also encouragingly, a very similar diffusivity is obtained by fitting the relaxation curves after the voltage is switched off to a diffusion model (Figure S7). The experimentally obtained diffusivity resembles the literature value for $[Fe(CN)_6]^{3-}$ used as an input for the simulation (Table S2).[6] This finding suggests that the effective diffusivity measured for such a multicomponent system is dominated by the slowest charged species, analogous to the constraint of charge neutrality on charge carrier transport in semiconductors where the electrostatic attraction of the slowest species "slows" down the others.[6,53]

We have established that detecting solute concentration-induced differences in index of refraction with high sensitivity enables direct optical imaging of solution-phase ion distributions in the electrolyte and their spatiotemporal evolution. This capability not only allows for quantitative, model-free extraction of ion transport parameters from experimental data but also allows imaging of dynamic responses to electrochemical perturbation with sub-mM sensitivity at millisecond and submicrometer resolution. In particular, we have benchmarked this approach using a scenario in which an applied perturbation performs chemistry to alter a solution's makeup while maintaining the ability to determine intrinsic ion diffusivity. Directly probing solution-phase ion transport with high spatial and temporal resolution in native environments without added labels or invasive probes is crucial to understanding the myriad phenomena that rely on ion transport.

We envision a series of far-reaching implications of the methodology developed and validated herein. First, the methodology set forth uses a highly general label-free contrast mechanism that should enable spatiotemporal detection of solutes *and* their transport, as virtually all solutes—including monatomic ions and nonionic species—perturb at least the real part of the refractive index of their surroundings.[42,43] Even though the characteristic signal strengths that we observe in solution are ∼100× smaller than those of ions observed in solid matrices,[41,54] with careful calibration and a sensitive camera, one could envision a complete chemical analysis of electrochemical products being generated *in situ* at an electrode surface. Even the sensitivity to simple salts such as K_2SO_4 should be in the mM range in the present configuration (Figure 2a, Table S1). The sensitivity of the method is not so much dependent on the optical response to different ions, which scales with K_i, as it is to the net sum of ion contributions as a function of space and time; for example, $[Fe(CN)_6]^{3-}$ and $[Fe(CN)_6]^{4-}$ each relatively strongly change the index of refraction of a solution, but their contributions are nearly equal and opposite, and the detection presented in Figure 2 requires sensitivity to this small difference, as exemplified by our measurement-fed model of the individual contributions of the different solution components (Figure S4). This sensitivity is not intrinsic to the method and could conceivably be enhanced by optimizing factors such as the substrate and solution refractive indices or the detector. In the present sample, we estimate that the method is sensitive to probe current densities down to ∼10 mA/cm^2 on the shortest length and time scales and down to ∼10^{-1} mA/cm^2 at long times, but the overall range of sensitivity could be extended almost arbitrarily by adjusting the field-of-view, electrochemical cell size and frame rate (see SI for further discussion). Moreover, this strategy is highly accessible because not only is the contrast mechanism general but only modest alterations to a standard optical microscope are required to image electrolyte distributions. As such, we expect this approach will be a valuable label-free probe for ionic transport in a wide range of physical, chemical, and biological contexts, including product formation and collection in (photo)electrochemical energy conversion,[1,3] water splitting,[39] phototriggered ion transport,[55] ion transport in soft matter,[2] aqueous battery function, dissolution dynamics after proper calibration of the refractive index near saturation, microfluidic ion flow, bioelectronic device function, or even label-free electrophysiology dynamics.[4] It could also be readily combined with established strategies to optically detect oxygen and hydrogen evolution,[39] especially since the sensitivity required to see gaseous products is orders of magnitude lesser than what we have demonstrated for solution-phase species, and to potentially probe three-dimensional ion transport in such contexts.[49,56] Second, the MSE analysis used here could serve as a general approach to reveal nondiffusive behavior or spatially dependent transport parameters. Specifically, similar to the case for carrier transport probed by spatiotemporal methods,[51,52] deviations from diffusive transport manifest as nonlinear MSE curves that would be readily discerned. Finally, directly visualizing ion distributions and mass transport spatiotemporally in two dimensions grants information about the impact of electrode structure or heterogeneity and the commensurately local electrode activity that is not accessible from conventional current−voltage measurements that average over the system. As a simple example, variations in the present electrochemical cell's electrode deposition reveal regions of high local activity (Figure S8). Even though the total current integrated over the anode and cathode must be balanced, this constraint is broken locally when an electrode on one side of the channel has a larger local surface area than the one opposite it (Figure S8). The ability to resolve such variations should facilitate electrochemical device design and optimization.

■ ASSOCIATED CONTENT

Supporting Information

The Supporting Information is available free of charge at https://pubs.acs.org/doi/10.1021/acsenergylett.3c00129.

https://doi.org/10.1021/acsenergylett.3c00129
ACS Energy Lett. 2023, 8, 1785−1792

Experimental details, optical spectra, refractive index versus concentration coefficients, simulation details, simulated concentration profiles, component contributions to differential signal, chronoamperometry measurement and simulation, alternating voltage experiments, diffusion modeling, and examples of heterogeneous behavior within the electrochemical cell (PDF)

AUTHOR INFORMATION

Corresponding Authors

Naomi S. Ginsberg − *Department of Chemistry, University of California, Berkeley, California 94720, United States; Liquid-Sunlight Alliance and Materials Science Division and Molecular Biophysics and Integrated Bioimaging Division, Lawrence Berkeley National Laboratory, Berkeley, California 94720, United States; Department of Physics and STROBE, National Science Foundation Science and Technology Center, University of California Berkeley, Berkeley, California 94720, United States; Kavli Energy NanoSciences Institute at Berkeley, Berkeley, California 94720, United States;* orcid.org/0000-0002-5660-3586; Email: nsginsberg@berkeley.edu

James K. Utterback − *Department of Chemistry, University of California, Berkeley, California 94720, United States; Liquid-Sunlight Alliance, Lawrence Berkeley National Laboratory, Berkeley, California 94720, United States;* Present Address: J.K.U.: Sorbonne Université, CNRS, Institut des NanoSciences de Paris, INSP, 75005 Paris, France; orcid.org/0000-0002-2926-841X; Email: james.utterback@insp.jussieu.fr

Authors

Alex J. King − *Liquid-Sunlight Alliance and Energy Conversion Group, Lawrence Berkeley National Laboratory, Berkeley, California 94720, United States; Department of Chemical and Biomolecular Engineering, University of California, Berkeley, California 94720, United States;* orcid.org/0000-0002-3156-1607

Livia Belman-Wells − *Liquid-Sunlight Alliance, Lawrence Berkeley National Laboratory, Berkeley, California 94720, United States; Department of Physics, University of California Berkeley, Berkeley, California 94720, United States*

David M. Larson − *Liquid-Sunlight Alliance, Lawrence Berkeley National Laboratory, Berkeley, California 94720, United States;* Present Address: D.M.L.: Twelve, Berkeley, California 94710, United States

Leo M. Hamerlynck − *Department of Chemistry, University of California, Berkeley, California 94720, United States*

Adam Z. Weber − *Liquid-Sunlight Alliance and Energy Conversion Group, Lawrence Berkeley National Laboratory, Berkeley, California 94720, United States;* orcid.org/0000-0002-7749-1624

Complete contact information is available at: https://pubs.acs.org/10.1021/acsenergylett.3c00129

Notes

The authors declare no competing financial interest.

ACKNOWLEDGMENTS

We are grateful to Frédéric Kanoufi, Gerd Rosenblatt, Frances Houle, Steve Harris, Milan Delor, Hannah Weaver and other Ginsberg Group members for helpful discussions. The custom microfluidic electrochemical cell was fabricated by Microfluidics Foundry based in Berkeley California. Instrument development was supported by STROBE, a National Science Foundation Science and Technology Center under grant no. DMR 1548924, and the application to electrochemistry was supported by Liquid Sunlight Alliance, which is supported by the U.S. Department of Energy, Office of Science, Office of Basic Energy Sciences, Fuels from Sunlight Hub under Award Number DE-SC0021266. J.K.U. acknowledges support from the Arnold O. Beckman Postdoctoral Fellowship in Chemical Sciences from the Arnold and Mabel Beckman Foundation. A.J.K. acknowledges funding from the National Science Foundation Graduate Research Fellowship under Grant No. DGE 2146752. L.M.H. acknowledges a National Defense Science and Engineering Graduate Fellowship. N.S.G. acknowledges a David and Lucile Packard Foundation Fellowship for Science and Engineering and a Camille and Henry Dreyfus Teacher-Scholar Award.

REFERENCES

(1) Modestino, M. A.; Hashemi, S. M. H.; Haussener, S. Mass Transport Aspects of Electrochemical Solar-Hydrogen Generation. *Energy Environ. Sci.* **2016**, *9* (5), 1533−1551.

(2) Bui, J. C.; Digdaya, I.; Xiang, C.; Bell, A. T.; Weber, A. Z. Understanding Multi-Ion Transport Mechanisms in Bipolar Membranes. *ACS Appl. Mater. Interfaces* **2020**, *12* (47), 52509−52526.

(3) King, A. J.; Bui, J. C.; Bell, A. T.; Weber, A. Z. Establishing the Role of Operating Potential and Mass Transfer in Multicarbon Product Generation for Photoelectrochemical CO_2 Reduction Cells Using a Cu Catalyst. *ACS Energy Lett.* **2022**, *7* (8), 2694−2700.

(4) Zhou, Y.; Liu, E.; Müller, H.; Cui, B. Optical Electrophysiology: Toward the Goal of Label-Free Voltage Imaging. *J. Am. Chem. Soc.* **2021**, *143* (28), 10482−10499.

(5) Bard, A. J.; Faulkner, L. R. *Electrochemical Methods: Fundamentals and Applications*, 2nd ed.; Wiley: New York, 2001.

(6) Newman, J. S.; Balsara, N. P. *Electrochemical Systems*, 4th ed.; Wiley: Hoboken, NJ, 2019.

(7) Bui, J. C.; Lees, E. W.; Pant, L. M.; Zenyuk, I. V.; Bell, A. T.; Weber, A. Z. Continuum Modeling of Porous Electrodes for Electrochemical Synthesis. *Chem. Rev.* **2022**, *122* (12), 11022−11084.

(8) Weber, A. Z.; Newman, J. Modeling Transport in Polymer-Electrolyte Fuel Cells. *Chem. Rev.* **2004**, *104* (10), 4679−4726.

(9) Mistry, A.; Srinivasan, V.; Steinrück, H. Characterizing Ion Transport in Electrolytes via Concentration and Velocity Profiles. *Adv. Energy Mater.* **2023**, *13*, 2203690.

(10) Fracastoro-Decker, M.; Decker, F. The Mirage Effect under Controlled Current Conditions. *J. Electroanal. Chem. Interfacial Electrochem.* **1989**, *266* (2), 215−225.

(11) Kragt, H. J.; Smith, C. P.; White, H. S. Refractive Index Mapping of Concentration Profiles. *J. Electroanal. Chem. Interfacial Electrochem.* **1990**, *278* (1−2), 403−407.

(12) O'Brien, R. N.; Saville, P. M. Transient Interfacial Concentration at a Notched Electrode by Laser Interferometry. *J. Electrochem. Soc.* **1993**, *140* (1), 122−127.

(13) Li, Q.; White, H. S. Interferometric Measurement of Depletion Layer Structure and Voltammetric Data in Concentrated Organic Redox Solutions. *Anal. Chem.* **1995**, *67* (3), 561−569.

(14) Shearing, P.R.; Howard, L.E.; Jørgensen, P.S.; Brandon, N.P.; Harris, S.J. Characterization of the 3-Dimensional Microstructure of a Graphite Negative Electrode from a Li-Ion Battery. *Electrochem. Commun.* **2010**, *12* (3), 374−377.

(15) Ebejer, N.; Güell, A. G.; Lai, S. C. S.; McKelvey, K.; Snowden, M. E.; Unwin, P. R. Scanning Electrochemical Cell Microscopy: A Versatile Technique for Nanoscale Electrochemistry and Functional Imaging. *Annu. Rev. Anal. Chem.* **2013**, *6* (1), 329−351.

(16) Holtz, M. E.; Yu, Y.; Gunceler, D.; Gao, J.; Sundararaman, R.; Schwarz, K. A.; Arias, T. A.; Abruña, H. D.; Muller, D. A. Nanoscale Imaging of Lithium Ion Distribution During In Situ Operation of Battery Electrode and Electrolyte. *Nano Lett.* **2014**, *14* (3), 1453−1459.
(17) LaManna, J. M.; Chakraborty, S.; Gagliardo, J. J.; Mench, M. M. Isolation of Transport Mechanisms in PEFCs Using High Resolution Neutron Imaging. *Int. J. Hydrog. Energy* **2014**, *39* (7), 3387−3396.
(18) Teng, X.; Huang, Q.; Dharmawardhana, C. C.; Ichiye, T. Diffusion of Aqueous Solutions of Ionic, Zwitterionic, and Polar Solutes. *J. Chem. Phys.* **2018**, *148* (22), 222827.
(19) Welch, A. J.; Fenwick, A. Q.; Böhme, A.; Chen, H.-Y.; Sullivan, I.; Li, X.; DuChene, J. S.; Xiang, C.; Atwater, H. A. *Operando* Local pH Measurement within Gas Diffusion Electrodes Performing Electrochemical Carbon Dioxide Reduction. *J. Phys. Chem. C* **2021**, *125* (38), 20896−20904.
(20) Klett, M.; Giesecke, M.; Nyman, A.; Hallberg, F.; Lindström, R. W.; Lindbergh, G.; Furó, I. Quantifying Mass Transport during Polarization in a Li Ion Battery Electrolyte by In Situ ^{7}Li NMR Imaging. *J. Am. Chem. Soc.* **2012**, *134* (36), 14654−14657.
(21) Rey, I.; Bruneel, J.; Grondin, J.; Servant, L.; Lassègues, J. Raman Spectroelectrochemistry of a Lithium/Polymer Electrolyte Symmetric Cell. *J. Electrochem. Soc.* **1998**, *145* (9), 3034−3042.
(22) Amatore, C.; Bonhomme, F.; Bruneel, J.-L.; Servant, L.; Thouin, L. Mapping Dynamic Concentration Profiles with Micrometric Resolution near an Active Microscopic Surface by Confocal Resonance Raman Microscopy. Application to Diffusion near Ultramicroelectrodes: First Direct Evidence for a Conproportionation Reaction. *J. Electroanal. Chem.* **2000**, *484* (1), 1−17.
(23) Brissot, C.; Rosso, M.; Chazalviel, J.-N.; Lascaud, S. Concentration Measurements in Lithium/Polymer−Electrolyte/Lithium Cells during Cycling. *J. Power Sources* **2001**, *94* (2), 212−218.
(24) Harris, S. J.; Timmons, A.; Baker, D. R.; Monroe, C. Direct In Situ Measurements of Li Transport in Li-Ion Battery Negative Electrodes. *Chem. Phys. Lett.* **2010**, *485* (4−6), 265−274.
(25) Forster, J. D.; Harris, S. J.; Urban, J. J. Mapping Li+ Concentration and Transport via In Situ Confocal Raman Microscopy. *J. Phys. Chem. Lett.* **2014**, *5* (11), 2007−2011.
(26) Sahore, V.; Kreidermacher, A.; Khan, F. Z.; Fritsch, I. Visualization and Measurement of Natural Convection from Electrochemically-Generated Density Gradients at Concentric Microdisk and Ring Electrodes in a Microfluidic System. *J. Electrochem. Soc.* **2016**, *163* (4), H3135−H3144.
(27) Padilla, N. A.; Rea, M. T.; Foy, M.; Upadhyay, S. P.; Desrochers, K. A.; Derus, T.; Knapper, K. A.; Hunter, N. H.; Wood, S.; Hinton, D. A.; Cavell, A. C.; Masias, A. G.; Goldsmith, R. H. Tracking Lithium Ions via Widefield Fluorescence Microscopy for Battery Diagnostics. *ACS Sens.* **2017**, *2* (7), 903−908.
(28) Cheng, Q.; Wei, L.; Liu, Z.; Ni, N.; Sang, Z.; Zhu, B.; Xu, W.; Chen, M.; Miao, Y.; Chen, L.-Q.; Min, W.; Yang, Y. Operando and Three-Dimensional Visualization of Anion Depletion and Lithium Growth by Stimulated Raman Scattering Microscopy. *Nat. Commun.* **2018**, *9* (1), 2942.
(29) Roberts, T. D.; Yuan, R.; Xiang, L.; Delor, M.; Pokhrel, R.; Yang, K.; Aqad, E.; Marangoni, T.; Trefonas, P.; Xu, K.; Ginsberg, N. S. Direct Correlation of Single-Particle Motion to Amorphous Microstructural Components of Semicrystalline Poly(Ethylene Oxide) Electrolytic Films. *J. Phys. Chem. Lett.* **2020**, *11* (12), 4849−4858.
(30) Wang, K.; Behdani, B.; Silvera Batista, C. A. Visualization of Concentration Gradients and Colloidal Dynamics under Electrodiffusiophoresis. *Langmuir* **2022**, *38* (18), 5663−5673.
(31) Wang, Y.; Yang, Q.; Su, B. Spatially Resolved Electrochemistry Enabled by Thin-Film Optical Interference. *Chem. Commun.* **2020**, *56* (82), 12359−12362.
(32) Cheng, Q.; Jin, T.; Miao, Y.; Liu, Z.; Borovilas, J.; Zhang, H.; Liu, S.; Kim, S.-Y.; Zhang, R.; Wang, H.; Chen, X.; Chen, L.-Q.; Li, J.; Min, W.; Yang, Y. Stabilizing Lithium Plating in Polymer Electrolytes by Concentration-Polarization-Induced Phase Transformation. *Joule* **2022**, *6* (10), 2372−2389.
(33) Feinleib, J. Electroreflectance in Metals. *Phys. Rev. Lett.* **1966**, *16* (26), 1200−1202.
(34) McIntyre, J. D. E. Electrochemical Modulation Spectroscopy. *Surf. Sci.* **1973**, *37*, 658−682.
(35) Kanoufi, F. Electrochemistry and Optical Microscopy. In *Encyclopedia of Electrochemistry*; Bard, A. J., Ed.; Wiley, 2021; pp 1−80. DOI: 10.1002/9783527610426.bard030108.
(36) Lemineur, J.-F.; Wang, H.; Wang, W.; Kanoufi, F. Emerging Optical Microscopy Techniques for Electrochemistry. *Annu. Rev. Anal. Chem.* **2022**, *15* (1), 57−82.
(37) Shan, X.; Patel, U.; Wang, S.; Iglesias, R.; Tao, N. Imaging Local Electrochemical Current via Surface Plasmon Resonance. *Science* **2010**, *327* (5971), 1363−1366.
(38) Lemineur, J.-F.; Noël, J.-M.; Combellas, C.; Kanoufi, F. Optical Monitoring of the Electrochemical Nucleation and Growth of Silver Nanoparticles on Electrode: From Single to Ensemble Nanoparticles Inspection. *J. Electroanal. Chem.* **2020**, *872*, 114043.
(39) Ciocci, P.; Lemineur, J.-F.; Noël, J.-M.; Combellas, C.; Kanoufi, F. Differentiating Electrochemically Active Regions of Indium Tin Oxide Electrodes for Hydrogen Evolution and Reductive Decomposition Reactions. An In Situ Optical Microscopy Approach. *Electrochim. Acta* **2021**, *386*, 138498.
(40) Namink, K.; Meng, X.; Koper, M. T. M.; Kukura, P.; Faez, S. Electric-Double-Layer-Modulation Microscopy. *Phys. Rev. Appl.* **2020**, *13* (4), 044065.
(41) Merryweather, A. J.; Schnedermann, C.; Jacquet, Q.; Grey, C. P.; Rao, A. Operando Optical Tracking of Single-Particle Ion Dynamics in Batteries. *Nature* **2021**, *594* (7864), 522−528.
(42) An, N.; Zhuang, B.; Li, M.; Lu, Y.; Wang, Z.-G. Combined Theoretical and Experimental Study of Refractive Indices of Water−Acetonitrile−Salt Systems. *J. Phys. Chem. B* **2015**, *119* (33), 10701−10709.
(43) Li, M.; Zhuang, B.; Lu, Y.; Wang, Z.-G.; An, L. Accurate Determination of Ion Polarizabilities in Aqueous Solutions. *J. Phys. Chem. B* **2017**, *121* (26), 6416−6424.
(44) Celebrano, M.; Kukura, P.; Renn, A.; Sandoghdar, V. Single-Molecule Imaging by Optical Absorption. *Nat. Photonics* **2011**, *5* (2), 95−98.
(45) Ortega-Arroyo, J.; Kukura, P. Interferometric Scattering Microscopy (iSCAT): New Frontiers in Ultrafast and Ultrasensitive Optical Microscopy. *Phys. Chem. Chem. Phys.* **2012**, *14* (45), 15625.
(46) Daum, P. H.; Enke, C. G. Electrochemical Kinetics of the Ferri-Ferrocyanide Couple on Platinum. *Anal. Chem.* **1969**, *41* (4), 653−656.
(47) Redner, S. *A Guide to First-Passage Processes*; Cambridge University Press: Cambridge, 2001.
(48) Zhu, T.; Snaider, J. M.; Yuan, L.; Huang, L. Ultrafast Dynamic Microscopy of Carrier and Exciton Transport. *Annu. Rev. Phys. Chem.* **2019**, *70* (1), 219−244.
(49) Delor, M.; Weaver, H. L.; Yu, Q.; Ginsberg, N. S. Imaging Material Functionality through Three-Dimensional Nanoscale Tracking of Energy Flow. *Nat. Mater.* **2020**, *19* (1), 56−62.
(50) Schnedermann, C.; Sung, J.; Pandya, R.; Verma, S. D.; Chen, R. Y. S.; Gauriot, N.; Bretscher, H. M.; Kukura, P.; Rao, A. Ultrafast Tracking of Exciton and Charge Carrier Transport in Optoelectronic Materials on the Nanometer Scale. *J. Phys. Chem. Lett.* **2019**, *10* (21), 6727−6733.
(51) Ginsberg, N. S.; Tisdale, W. A. Spatially Resolved Photogenerated Exciton and Charge Transport in Emerging Semiconductors. *Annu. Rev. Phys. Chem.* **2020**, *71* (1), 1−30.
(52) Utterback, J. K.; Sood, A.; Coropceanu, I.; Guzelturk, B.; Talapin, D. V.; Lindenberg, A. M.; Ginsberg, N. S. Nanoscale Disorder Generates Subdiffusive Heat Transport in Self-Assembled Nanocrystal Films. *Nano Lett.* **2021**, *21* (8), 3540−3547.
(53) Sze, S. M.; Ng, K. K. *Physics of Semiconductor Devices*, 3rd ed.; Wiley-Interscience: Hoboken, NJ, 2007.

(54) Wan, J.; Xu, Y.; Ozdemir, B.; Xu, L.; Sushkov, A. B.; Yang, Z.; Yang, B.; Drew, D.; Barone, V.; Hu, L. Tunable Broadband Nanocarbon Transparent Conductor by Electrochemical Intercalation. *ACS Nano* **2017**, *11* (1), 788−796.
(55) White, W.; Sanborn, C. D.; Fabian, D. M.; Ardo, S. Conversion of Visible Light into Ionic Power Using Photoacid-Dye-Sensitized Bipolar Ion-Exchange Membranes. *Joule* **2018**, *2* (1), 94−109.
(56) Pandya, R.; Valzania, L.; Dorchies, F.; Xia, F.; Hugh, J. M.; Mathieson, A.; Tan, J. H.; Parton, T. G.; De Volder, M.; Tarascon, J.-M.; Gigan, S.; de Aguiar, H. B.; Grimaud, A. Three-Dimensional Operando Optical Imaging of Single Particle and Electrolyte Heterogeneities inside Li-Ion Batteries. *arXiv (Materials Science)*, June 27, **2022**, ver. 1. DOI: 10.48550/arXiv.2207.13073 (accessed February 20, 2023).

https://doi.org/10.1021/acsenergylett.3c00129
ACS Energy Lett. 2023, 8, 1785−1792